physica status solidi a
www.pss-a.com

Micro-Particle Induced X-ray Emission Study of Lead-Free and Lead-Based Solders and Interactions with Copper Wires

Harry J. Whitlow and Gyula Nagy*

Pb-free electrical solders, such as Cu–Sn alloys, work well for reflow soldering under tightly controlled conditions. Hand soldering, however, often results in poor quality joints compared to conventional Pb–Sn solders. To investigate this under realistic workshop conditions, micro-particle induced X-ray emission (micro-PIXE) with 2 MeV protons has been employed. Commercial flux-cored Cu–Sn and Pb–Sn solder wires are studied. Solder blobs under two cooling conditions as well as tinning Restriction of Hazardous Substances (RoHS)-compliant and legacy component wires are investigated. The results show that the long heating and slow cooling of Cu–Sn solder blobs lead to formation of an acicular precipitate that can be ascribed to Cu_6Sn_5. Pb–Sn solder under the same conditions shows phase separation with regions of high Sn and regions with high Pb. In the case of rapidly cooled blobs where a shiny surface is produced, no phase separation in either solder is observed. Tinning of RoHS-compliant and legacy Cu component wires with the two solders produce significantly different interfacial depth profiles with varying degrees of grading, indicative of intermetallic phase formation.

1. Introduction

The Global Electronics Industry is a major industrial sector with a product value of $1191.2 billion in 2020.[1] Environmental and health concerns lead to the Restriction of the use of Hazardous Substances in electrical and electronic equipment (RoHS) Directive.[2] This limits the use of ten hazardous substances in electrical and electronic equipment and devices. Soldered joints are pivotal for the electronics industry because of their very wide application for electrical interconnections and mechanical fixtures. Prior to the RoHS Directive, Pb–Sn solders were widely used across the entire electronics industry. The implementation of the RoHS Directive requiring a maximum of 1‰ by mass of lead (Pb) in electronic products leads to the replacement of Pb–Sn solders with Pb-free alternatives such as electrically conductive adhesives based on metal particles[3,4] or carbon nanotubes[5] and Pb-free solders.[6–10] Modern electronics production is largely based on printed circuit boards with surface mount device (SMD) and reflow soldering using special alloys. It follows that uniform high-quality soldering joints play a key role in the economics of electronic manufacturing. This is because a single circuit board can have 200–1000 soldered interconnects and a single failed soldered interconnect can require that an assembled board with a high economic value of components must be discarded or reworked. In addition to this, hand soldering also plays an important role for prototyping as well as interconnecting cables, printed circuit board, and connectors. The present study stemmed from interest to understand workshop observations that hand soldering with Cu–Sn (Pb-free) solder is less satisfactory than with Pb–Sn solders because the Cu–Sn solder has a tendency to form poor-quality dull "dry" joints.

Fundamentally, soldering involves intermetallic reactions where a low melting point liquid phase partially dissolves the metals to be joined (wetting) which solidifies on cooling to form metal-1/solder/metal-2 interface structures. These are generally mechanically strong because the solder "wets" the surface so that on cooling the solder atoms form metallic bonds with the atoms of the substrate. Pure tin is unsuitable as a solder because of whisker growth and "tin-pest" which is a consequence of an allotropic transformation from body-centered tetragonal β white-tin phase below 13.2 °C to an adamantine α gray-tin phase with an accompanying 28% volume expansion.[7] To overcome this difficulty, a Cu–Sn (Cu 0.7 mass%, Sn bal) alloy is used. This alloy (hereafter referred to as Cu–Sn solder) represents an important RoHS-compatible solder which is often used for hand soldering. The binary Cu–Sn alloy system is also important because ternary alloys with, e.g., Ag are used to make commercial low-melting

H. J. Whitlow
Tandem Laboratory
Uppsala University
Box 529, 75121 Uppsala, Sweden
E-mail: harry.whitlow@physics.uu.se, h.j.whitlow@fys.uio.no

H. J. Whitlow
Norwegian Micro- and NanoFabrication Facility laboratory
The Department of Physics
University of Oslo
Po. Box 1048, Blindern, N-0316 Oslo, Norway

G. Nagy
Department of Physics and Astronomy
Uppsala University
Box 516, 75120 Uppsala, Sweden

The ORCID identification number(s) for the author(s) of this article can be found under https://doi.org/10.1002/pssa.202200432.

DOI: 10.1002/pssa.202200432

temperature Pb-free solders because the addition of Cu stabilizes the β phase.[7,9,11,12]

There is an ongoing migration in electronics prototype workshops from hand-soldered joints for through-hole components toward smaller and thinner joints using reflow techniques. For this and commercial manufacture, there is a strive to improve the reliability of soldered joints both with respect to reliability in fabrication and long-term durability. The formation of interfacial intermetallic compounds (IMC) is detrimental[13] because of stress-induced cracking and formation of Kirkandall voids. Approaches to mitigate this include application of thin Ni-based diffusion barriers[13,14] and incorporation of Ni particles into the solder.[15]

1.1. Application of Micro-PIXE for Study of Soldering

The phase diagrams of the Cu–Sn[16] and Pb–Sn[17] as well as the ternary Pb–Sn–Cu[18] phase diagram indicate which phases are present at thermodynamic equilibrium. Soldering of copper wires represents an off-equilibrium dissolution-limited situation where unreacted Cu substrate and solder are present in excess. The Cu–Sn phase diagram[16] reveals that the Cu–Sn eutectic is close to 0.7 mass% Cu. The outcome of soldering can be strongly influenced by even trace amounts of impurities. Thus, to study joints made with Pb–Sn solder with a Cu substrate, the analytical method should be capable of measuring subeutectic levels of Cu in Sn. High analytical sensitivity is also required to study the fate of thin diffusion barrier layers discussed above as well as trace levels of impurity elements.

Micro-PIXE is a powerful ion beam analytical method for quantitative imaging and composition analysis of elements with atomic number >13. Micro-PIXE is conceptually similar to energy-dispersive X-ray (EDX) analysis but employs MeV protons or He ion beams.[19] Quantitative analysis using micro-PIXE[20,21] that was employed in this study has much higher sensitivities than EDX because the characteristic X-ray peaks are superposed on a much smaller background from bremsstrahlung, pulse pile-up, etc. Micro-PIXE has been used extensively in archaeometry studies to investigate soldering of, e.g., gold artifacts.[22–25] It has also been applied to study hazardous solder particles[26] and by one of us (H.J.W.) to study Cu–Sn phases and Hg loss during tribochemical interactions of dental amalgam.[27,28]

1.2. Goal and Scope of the Study

The goal of the study was to use micro-PIXE to quantitatively investigate the redistribution of major and minor elements during soldering under realistic workshop conditions by comparing two common rosin-cored electrical solders, a lead-free Sn–Cu alloy and a conventional Sn–Pb alloy.

2. Results

2.1. PIXE Spectra

The micro-PIXE X-ray spectra (**Figure 1**) of blobs of Cu–Sn and Pb–Sn alloy solder wires that were melted at a soldering tip temperature of 420 °C were used to determine the solder composition. Under these conditions, the blobs had a gray and rough surface giving a "dry" appearance. The melt data of Figure 1 exhibited a more uniform composition than the solder wires as discussed in Section 2.2. In this figure, the characteristic X-ray peaks from Br, Cu, Pb, and Sn are well separated. The fitted

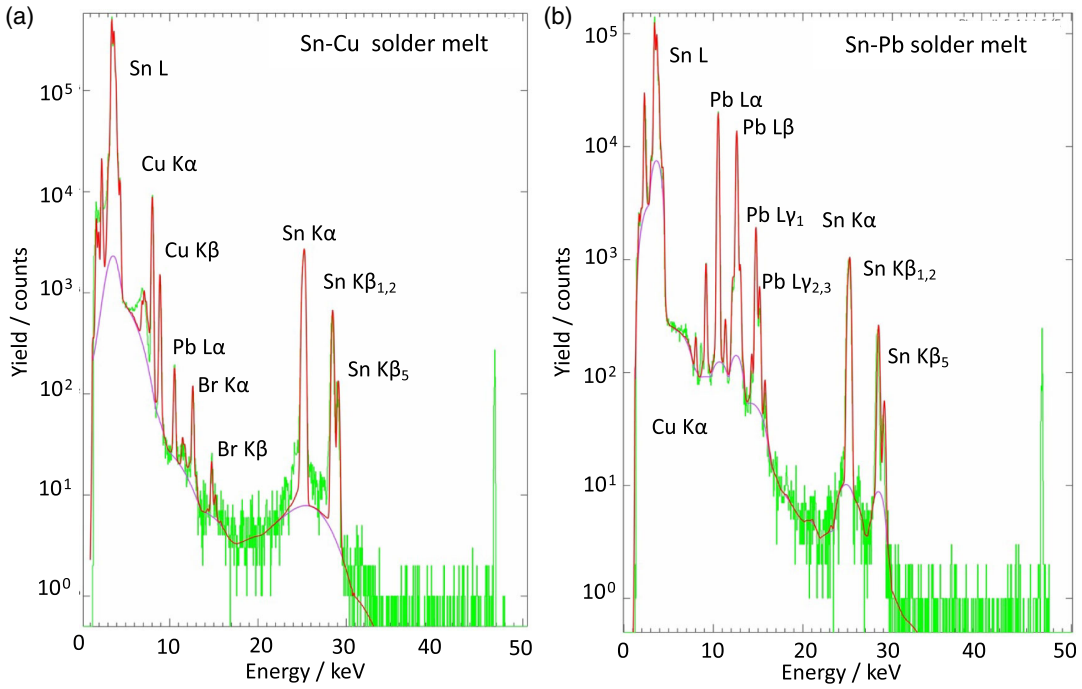

Figure 1. a,b) Micro-PIXE X-ray spectra for melted blobs of Cu–Sn (a) solder and Pb–Sn (b) solder melts analyzed with 2 MeV protons. The green, red, and purple lines denote the experimental data, fitted data, and background function, respectively.

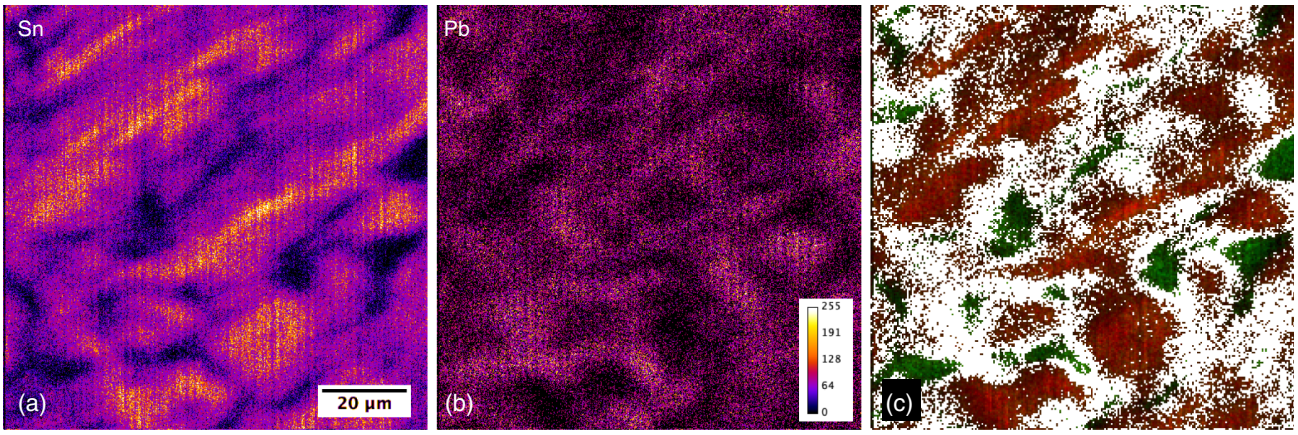

Figure 2. Elemental maps (contrast normalized) for as-received Sn–Pb solder wire. a) Sn and b) Pb elemental maps. (The color scale for (a) and (b) is shown in the inset of (b). c) Colocalized Sn and Pb (white channel), Sn (green channel), and Pb (red channel). The elemental concentration maps have been normalized (see text).

spectrum shown in Figure 1 was in close agreement with the experimental spectrum. The peaks were superposed on a background that is largely bremsstrahlung. In addition, a well-separated S Kα peak was observed. This originated from the embedding compound and was neglected in subsequent analysis. For both samples, the measured Cu, Sn, and Pb contents were significantly greater than the method detection limit (MDL). Characteristic X-rays from Br were observed from the Cu–Sn solder. In the Pb–Sn solder case, the Br signal did not exceed the MDL.

2.2. Analysis of Solder Wire

In **Figure 2**a,b, respectively, the elemental maps Sn and Pb for a 100 μm × 100 μm area of the as-received Pb–Sn wire are presented. The colocalization of Pb (red) and Sn (green) is shown in Figure 2c. This showed a morphology for the solder wire with regions of pure Pb, pure Sn, and Pb–Sn alloy. The corresponding images (not shown) for the as-received Cu–Sn solder wire were unremarkable with no discernible morphology and a composition corresponding closely to the solder melt.

2.3. Micro-PIXE of Solder Melts

The measured compositions of the solder melts determined from the data of Figure 1 are given in **Table 1**. For both samples, the measured Cu, Sn, and Pb contents exceeded the MDL. The Cu–Sn solder was in poor agreement with the manufacturers stated composition, whereas the Pb–Sn solder had an off-eutectic composition. A low level of Pb was detected in the Cu–Sn melted blob, but not in the as-received solder wire at concentrations above the MDL.

Table 1. Composition of melted solder blobs from PIXE by mass.

Type	Cu	Sn	Pb
Cu–Sn	2.29 ± 0.02%	97.48 ± 0.02%	2306 ± 100 ppm
MDL [ppm]	40	30	85
Pb–Sn	Detected	69.06 ± 0.3%	30.1 ± 0.22%
MDL [ppm]	155	197	96

The Cu and Sn concentration maps for the Cu–Sn solder are presented in **Figure 3**a,b. Inspection shows that although Sn and Cu were present throughout the melt, the Cu distribution was nonuniform and enhanced in acicular grains of ≈10 μm cross section and 100–200 μm in length. The acicular grains observed in Figure 3 exhibited no preferential orientation and form a 3D random network. These regions appear to have a Cu concentration that varies along the long axis.

The melted Pb–Sn solder blob elemental maps shown in **Figure 4** reveal that the Pb and Sn distributions are also inhomogeneous but on a much finer scale than for the Cu–Sn case. The Pb distribution is more uniform than for Sn. Colocalization studies confirmed the concentrations of Pb in Sn-rich regions and Sn in Pb-rich regions exceeded zero.

2.4. Effect of Melting Temperature on Cu–Sn Solder

In this series of tests, blobs of solder were quickly melted and cooled onto 0.3 mm aluminum foil to simulate the conditions of soldering a good joint without any interaction with the substrate. The temperature interval between samples in the series was 40 °C. **Figure 5** presents the elemental maps at the lowest and highest soldering tip temperatures. At all temperatures, the melt blobs exhibited a smooth, shiny surface appearance. The lowest temperature (260 °C) corresponded to where the soldering tip just overcame the combined thermal resistances and heat loss from the solder wire to achieve melting. Data at intermediate temperatures exhibited no evidence of phase separation and are not shown. A thin Sn and Cu containing layer is seen at some distance from the surface for all temperatures and appears detached from the bulk. Br was observed to be concentrated in this near-surface layer.

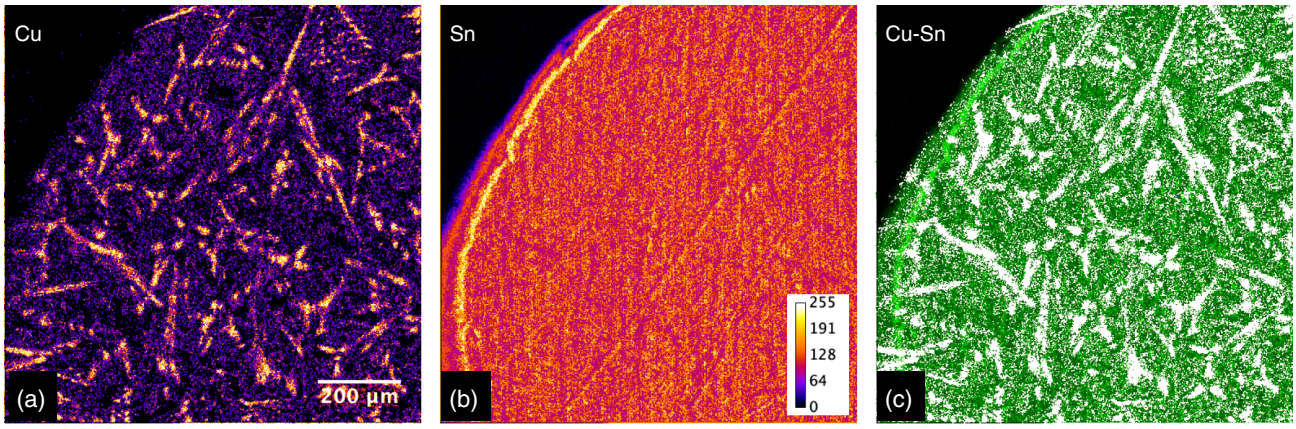

Figure 3. Cu–Sn solder melt under "dry joint" conditions. a) Cu, b) Sn, and c) Cu (red), Sn (green), colocalized Cu and Sn (white) Cu (red) and Sn (green). The elemental concentration maps have been normalized (see text).

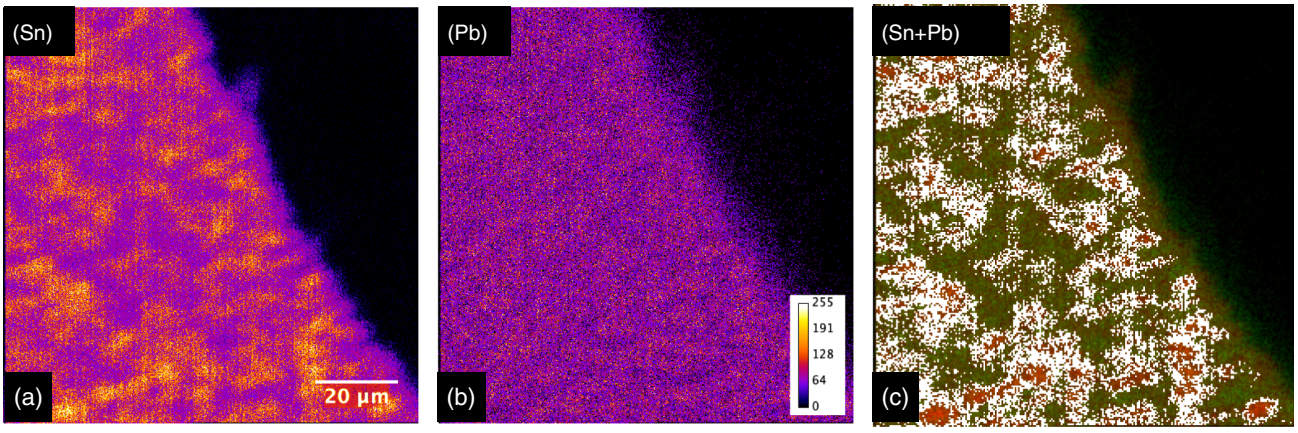

Figure 4. Sn–Pb solder melt under "dry joint" conditions. a) Sn, b) Pb, and c) colocalized Sn and Pb (white channel), Sn (green channel), and Pb (red channel). The Sn colocalization threshold was set to 37.5% of maximum intensity to reveal the Sn-rich phase. The elemental concentration maps have been normalized (see text).

2.5. Solder Interactions with Tinned Cu Wires

To investigate the interaction of the Pb-free and Sn–Pb solder with tinned copper wires, elemental concentration profiles were obtained using GeoPIXE[29–31] from the elemental maps, for mechanically polished samples where the polished surface plane lays along the axis of the wire. The depth profile along a radial direction was then obtained from a rectangular region as illustrated in **Figure 6**. The measured concentration profiles at 380 °C soldering tip temperature for both types of solder are presented for Cu wire from an RoHS-compliant and a legacy component in **Figure 7** and **8**, respectively. The concentration scales were normalised to 100 mass% Cu in the bulk of the copper wires.

3. Discussion of Results

3.1. Solder Wire

The composition of the Cu–Sn solder wire was observed to be closely identical to that of the melt (Section 3.2). Furthermore, the Cu and Sn elemental maps (not shown here) were featureless. The elemental maps for the Pb–Sn solder (Figure 4) showed an inhomogeneous elemental concentration morphology. Colocalization investigation showed regions of pure Sn and pure Pb interspersed in regions with both Sn and Pb present. This is different from what is expected from the phase diagram which implies coexistence of α and β solid solution phases of Pb and Sn[17] (probably with an eutectic morphology). This situation might arise if the solder wire was fabricated by extrusion of a mixed powder. The large variations in the composition over the analyzed area gave rise to a composition that differed from the melt discussed below (Section 3.2).

3.2. Solder Melts

The measured composition (Table 1) of the melted Cu–Sn solder blob was not in good agreement with the manufacturers stated composition for the Cu–Sn solder (0.7 mass% Cu, bal. Sn). This may be associated with production variations. A further source for the enhanced Cu concentration may be dissolution of the Cu soldering tip used to melt the sample. It was also notable that Pb was present (0.23 mass%). This exceeds the RoHS limit[2] and

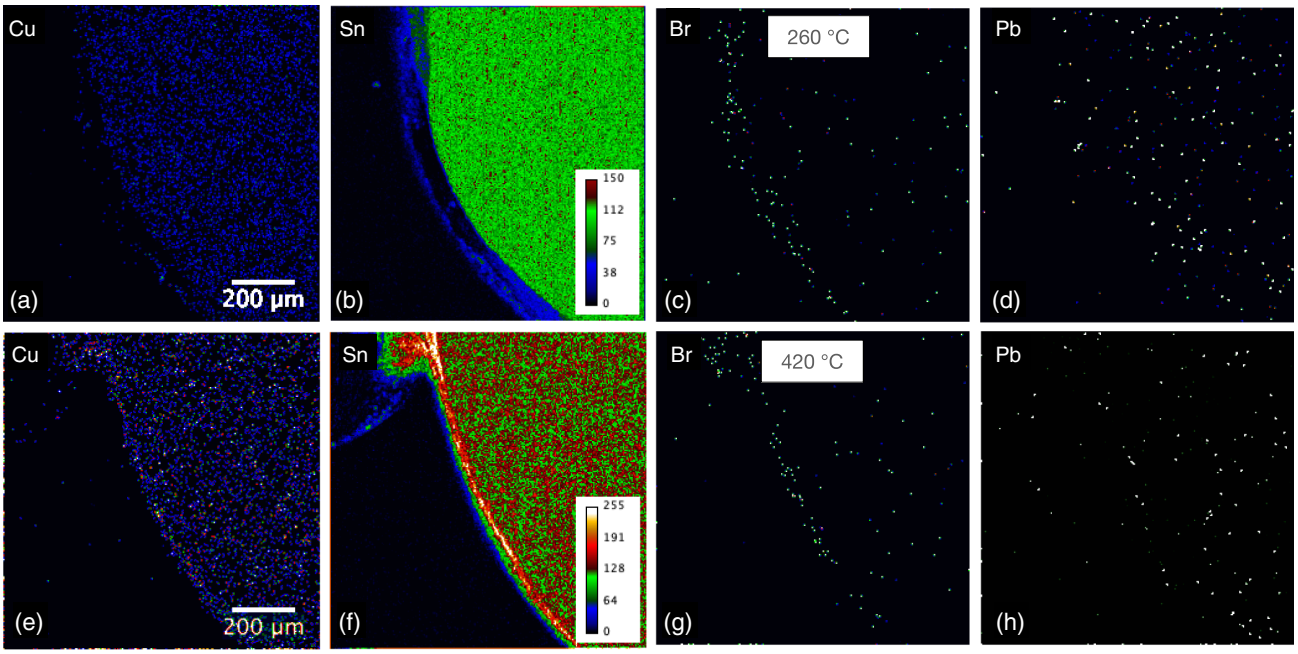

Figure 5. a–h) Elemental maps for Cu–Sn solder melted at 260 °C (a–d) and 420 °C (e–h) under "good joint" conditions. To facilitate comparison each image has been contrast normalized. (Note: the color scale is different to enhance visibility.).

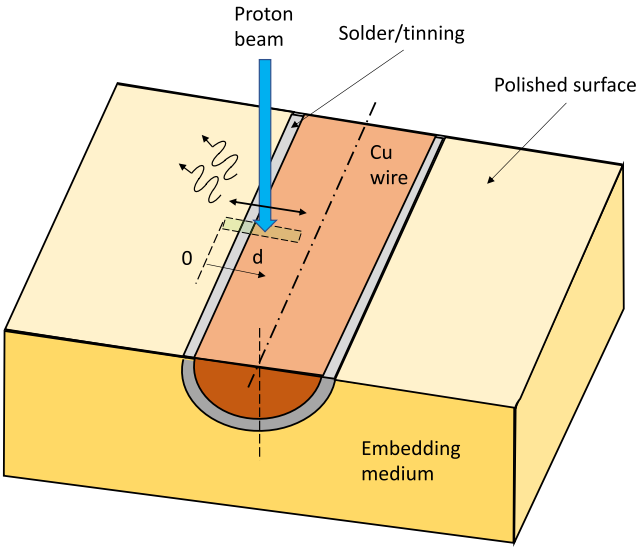

Figure 6. Configuration for measurement of the elemental depth profiles of soldered/tinned wires. Compositional analysis along the rectangular region yields the radial elemental depth profile.

was not observed in the as-received Cu–Sn solder wire. The Pb could have originated from Pb–Sn solder contamination of the soldering iron tip that was redissolved into the molten solder. Another possible Pb source is dissolution of the tip itself because some copper grades contain 1–3 mass% Pb.

The elemental maps of Figure 3 show that for Cu–Sn solder, copper was distributed throughout the melt but concentrated in acicular Cu-rich grains. The overall composition was close to eutectic (Table 1). The Cu–Sn phase diagram[16,32] shows that above 408 °C the Cu_6Sn_5 η phase is in equilibrium with Sn.[32] Above this temperature, the εCu_3Sn phase is also in equilibrium.[32] It is well known the morphology of a eutectic is highly dependent on the rate of freezing and chemical composition.[33,34] Attempts were made using GeoPIXE to measure the composition of the acicular grains from the elemental maps. However, the results were uncertain and more Sn rich than the η phase predicted by the equilibrium phase diagram. The composition measurement could be biased toward Sn-rich because the cross section of the grains was similar to the sensitive depth for PIXE analysis resulting in an uncontrolled sampling of regions of differing composition. It could be that the observed concentration variations along the length of the grain of η phase also arise for the same reason because the acicular grains form a random 3D network. The tentative conclusion is that the acicular grains are the Cu_6Sn_5 η phase predicted by the equilibrium phase diagram.[16,32] However, we cannot rule out that these grains are also associated with the formation of Cu_3Sn.[7,32]

The Pb–Sn solder had an off-eutectic[17] composition with about ≈70 mass% Sn (Table 1)). This composition is commonly marketed as a multifunction solder with high shear and tensile stress. The Cu concentration was close to the MDL. The compositions differed from, but were not inconsistent with, the as-received solder wire. Figure 4a,b reveals that the Pb was uniformly distributed but the Sn was accumulated in small grains that also contain Pb. This was confirmed by the colocalized (Sn–Pb) image (Figure 4c). This is consistent with the measured Sn content (Table 1) exceeding the eutectic value of 61.9 mass%.[17] This alloy composition can be expected on cooling under equilibrium conditions to precipitate first as fine α-Pb particles in a pre-eutectic of β(Sn) at decomposes to eutectic + β-Sn along the liquidus line. Then the small Sn-rich

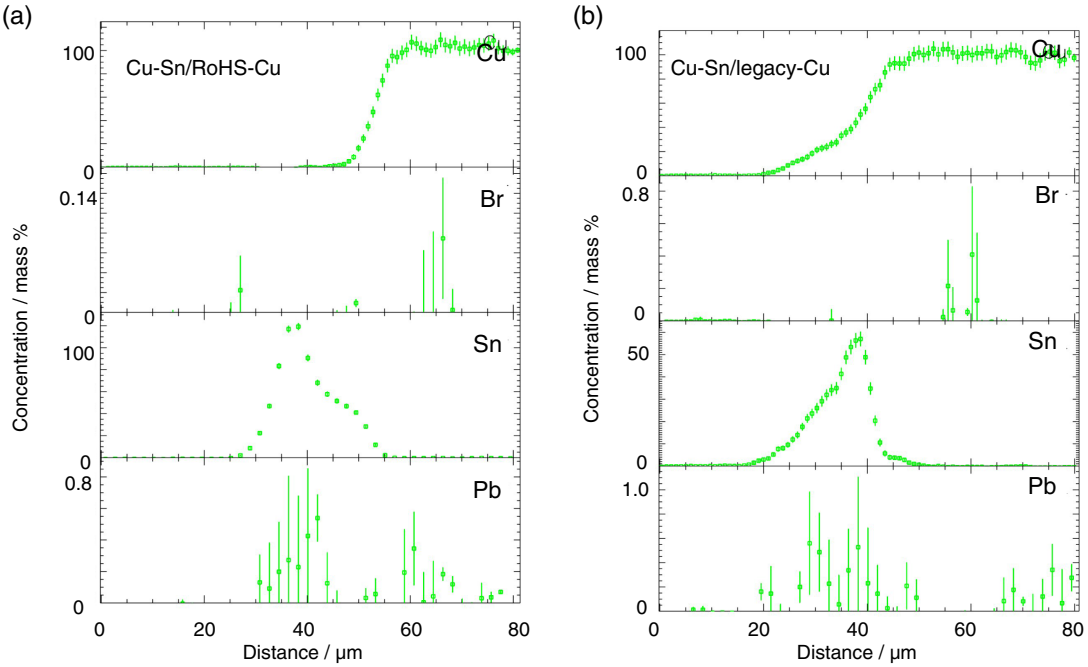

Figure 7. a,b) Elemental depth profiles for Cu–Sn solder on RoHS (a) and legacy-tinned (b) Cu wires.

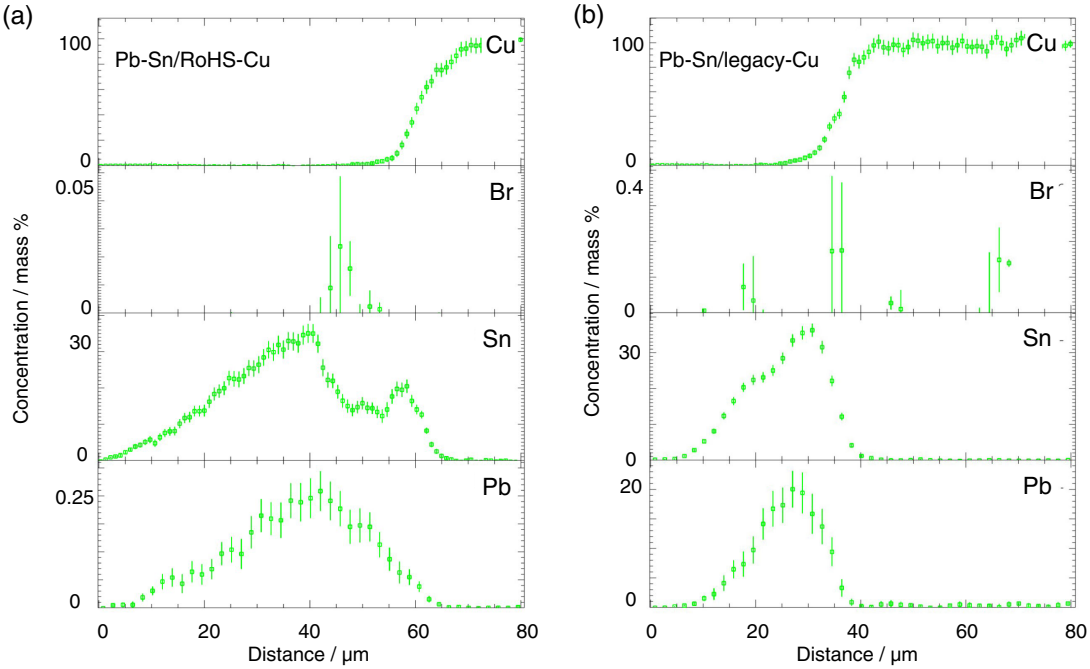

Figure 8. a,b) Elemental depth profiles for Pb–Sn solder on RoHS (a) and legacy-tinned (b) Cu wires.

grains could be assigned β-Sn. The uniform surrounding region is then small grains of α and β phases.[17]

3.2.1. Effect of Soldering Temperature on Cu–Sn Solder Melts

Figure 5 presents micro-PIXE elemental maps of cross sections of the good quality (rapidly heated and cooled) Cu–Sn solder blobs. The blobs had a shiny surface. This figure shows the images for the highest and lowest temperatures. Intermediate temperature data are not presented here because no detectable differences were observed at intermediate temperatures. Notably, there was no indication of the phase separation that was observed in the dry-joint case (Figure 3). The absence of a Cu-rich phase (likely, Cu_6Sn_5 η phase) implies that the formation of these grains on slow cooling is a likely

cause of the dull and rough surface of "dry joints" with Cu–Sn alloy.

3.2.2. Surface Interactions and Flux

The surface of the Cu–Sn solder melts exhibited a thin layer containing Cu and Sn that appears to be detached from the surface (Figure 5). Furthermore, Br was present in the surface region with trace amounts inside the solder blob. The origin of the Br is likely to be the flux core of the Cu–Sn solder which is based on rosin. This natural product is the residue, after light hydrocarbons have been distilled off, from pine resin.[35] It is mostly composed of abietic and pimaric acids. These acids serve to improve wetting of metal substrates by dissolution and disruption of interfacial oxides. Abietic and pimaric acid are not detectable by PIXE because they are hydrocarbons with only O as heteroatoms. Br is a likely additive to the flux to render it more active. (Given the adhesive nature of rosin and its solubility in alcohols, we could not discount the possibility that trace amounts can be carried over to other regions of the sample during the cleaning step.)

3.3. Interfacial Reactions with Tinned Copper Wires

An ideal interface between solder and a substrate is generally an abrupt junction. The formation of intermetallic compounds at the junction is considered undesirable because it can lead to stress-induced cracks with ageing.[14]

3.3.1. Cu–Sn Case

Figure 7a,b shows the elemental depth profiles of Cu, Br, Sn, and Pb that result from so-called "tinning" of Cu wire from an RoHS-compliant component (Figure 7a) and a legacy component (Figure 7b). The depth profiles are quite different. In Figure 7a, the Cu profile at the interface is sigmoid shaped. The presence of a shoulder Sn concentration might be attributed to formation of a graded junction with an intermetallic phase. The close to 100 mass% of Sn at the surface is indicative of an unreacted Cu–Sn solder at the surface. Br is observed in the bulk of the copper wire with the presumed contaminating Pb in both the Cu and Cu–Sn solder regions. Distinct from the Sn/Cu interface (≈55 μm), there is a plateau (≈45–50 μm).

For the case of the legacy Cu wire (Figure 7b), the Cu and Sn distributions exhibited a long tail extending toward the surface. This might be caused by surface roughness and/or surface oxidation. Br was only observed in the bulk of the Cu. As for (a), the Sn/Cu interface is sharp with a hint of the formation of a phase between the interface and surface. The Cu profile had a tentative indication of a sharp or sharp graded interface with a persistent tail extending toward the surface.

3.3.2. Pb–Sn Case

The results (Figure 8) for both the Pb–Sn/RoHS–Sn/Cu (a) and Pb–Sn/legacy–Sn/Cu (b) were indicative of complex interactions. In the Pb–Sn/RoHS–Cu case (Figure 8a), the Sn/Cu interface region extended over ≈30 μm with plateaus and kinks in the Cu and Sn distributions (Figure 8a). There is also a shoulder on the Pb distribution at ≈50 μm depth. Toward the surface, the Sn and Pb tailed off. This again might be attributed to roughening and surface oxides.

The Pb–Sn/legacy–Cu case (Figure 8b) was similar to that of the Pb–Sn/RoHS–Cu case (Figure 7, Section 3.3.1). The Sn/Cu and Pb/Cu junctions were more abrupt than Figure 7a. A near-surface plateau in the Sn profile at ≈25 μm was also observed, but plateaus were absent in the Pb profile. A surface Sn oxide phase could account for the near-surface Sn plateau.

Taken together the results of this section and Section 3.3.2 indicated that the outcome of "tinning" of the wires was highly variable and depended on if Cu–Sn or Pb–Sn solder was used and also the provenance of the wires.

3.4. Relevance of the Findings to Workshop Practice

As noted in Section 1.2, the study was performed under semi-controlled workshop conditions. The results discussed showed a large degree of variability in the outcome. Sections 3.2 and 3.1 show that at prolonged heating and slow cooling ("dry-joint" conditions) leads to the formation of acicular grains of Cu_6Sn5. These were likely the cause of a "dry" joint appearance. The results discussed in Section 3.2.1 showed that this grain growth was not observed with rapid cooling. Surface flux and oxide residues discussed in Section 3.2.2 may also affect joint appearance. Section 3.3.1 and 3.3.2 discuss the considerable difference observed in the tinning behavior. In this connection, it is noteworthy that there are literature reports that small quantities of alloying elements can have a significant impact on solder performance.[34] Likely previous use of the soldering tip for legacy Pb-based solders can have introduced levels of Pb (Figure 1, and Table 1) that can exceed the RoHS limit[2] into Pb-free solder confirms the need to use one set of soldering tools exclusively for Pb-free solder work. The observation discussed in Section 3.2.2 that Br was present as a potentially corrosive residue highlights the importance of removing flux residues after soldering. "Tinning" with Cu–Sn solder and Pb–Sn solder had very different interfacial reactions depending on the history of the pretinned copper wire. The implication of the large variations was that for soldering of stock components, the outcome can be unpredictable and some experimentation may be necessary to achieve good soldered joints with both Cu–Sn and conventional Pb–Sn solders.

4. Conclusions

The results showed that micro-PIXE is well suited to study compositional changes during the soldering process. This is particularly useful where small quantities of alloying elements can modify the soldering performance. The results showed that over a soldering tip temperature of 260–420 °C good quality solder blobs could be obtained by fabrication of the joint by rapid heating/cooling. Results for soldering pretinned copper wires showed with significant differences in the solder layer behavior depending on if a Cu–Sn or Pb–Sn solder was used and if the tinning on the Cu wire was RoHS compliant or a legacy tinned wire.

5. Experimental Section

Sample Preparation: As the objective was to study hand soldering using normal workshop practice conditions, the samples were prepared by a person with long experience in electronic construction. The solder alloys used in this study were taken from workshop supplies that were purchased from a local electronics component supplier. Both were 1 dia flux-cored solder wire. The Cu–Sn alloy had a stated composition of 0.7 mass% Cu 99.3 mass% Sn. The Pb–Sn alloy was legacy material from ≈1990 with unspecified composition. A standard thermostatically controlled soldering iron (LD 48: CFH Löt und gasgeräte GmbH) was used. As the soldering iron tip might have been exposed to Pb–Sn solder during maintenance work, it was cleaned prior to use. This was done by melting Pb-free solder on the tip at 420 °C and removing the molten solder on a wetted sponge. For the Pb–Sn, a separate ~420 °C soldering iron with a solid copper tip was used. The copper tip used for the Pb–Sn solder was filed prior to use so that a visibly clean copper surface was obtained and subsequently tinned. The blobs of solder representative of dry-joint conditions were heated for 1 min on a wood-backed 1 mm phenolic sheet with long heating through contact with the soldering iron at 420 °C and slow cooling (>1 min). The solder blob characteristics of a good soldered joint were made by rapid melting and cooling on a 0.3 mm-thick aluminum sheet.

To study the wetting of modern RoHS era components and components from the Pb–Sn era through-hole mounting resistors were used. The RoHS-compliant Cu wires were taken from a modern 0.125 W metal oxide resistor. The representative legacy Cu wire sample was taken from a 0.25 W carbon resistor which was ascertained to have been manufactured prior to 1970. After tinning with Pb-free or Pb–Sn solder at 380 °C, the wires were cut. The wires and solder blobs were placed in a plastic mold and embedded in rapid epoxy (Biltema 36-2448). This was selected because it had a hardness similar to the solders studied. After curing for 24 h, the samples were mechanically polished under flowing deionized water with carborundum paper from 180, 600, and 1200 grade. The polishing was done such that the wires were sectioned along their length to expose a cross section of the tinned layer as shown in Figure 6.

Micro-PIXE Analysis: The MeV ion microprobe in the Tandem Laboratory of Uppsala was used for the measurements with a 2 MeV proton beam.[36] This has a standard Oxford triplet quadrupole lens configuration with 220 mm working distance. Event-mode data collection was used a FAST ComTec MPA-3 data collection system with 7072T ADCs. This digitized the analogue signals from the Si–Li X-ray detector together with the raster scanning signals which were generated by a National Instruments PCI-e card configured to produce ramp waveforms. A 1 mm-thick PGT X-ray detector subtending ≈24 msr with a 12.5 μm Be window was used. A 72 μm thick mylar filter to prevent backscattered protons reaching the detector and attenuate low-energy X-rays that would otherwise dominate the spectrum. The fitted energy resolution was 187.9 keV FWHM for Cu Kα X-rays. The proton beam was focused to 2.6 μm × 1.6μm FWHM and the unsuppressed sample current was ≈0.2–0.3 nA. The X-ray detector was calibrated using 2.123 keV Mα_1 and 13.382 keV Lγ_1 characteristic X-rays from Au sample. The scan sizes at low and high magnification were calibrated using 120-mesh Ni and 1000-mesh Cu electron microscope grids, respectively.

Data Analysis: Analysis of the micro-PIXE data was carried out using the direct analysis method using the GeoPIXE code version 8.6z.[29–31] To overcome ill-controlled secondary electron emission from the sample in quantitative compositional analysis, the ion charge was fitted to a region of well-defined composition well inside the bulk of sample (e.g., 97.3 mass% Sn for the Pb-free solder, 100 mass% Cu inside the wire sections, and a sum of 100 mass% Pb + Sn for the Pb–Sn solder). Supplementary image analysis (contrast normalization, color colocalization[37]) was carried out using the ImageJ code.[38] To improve visibility and facilitate intercomparison of the lateral distributions, the elemental maps were converted to 8 bit gray-scale and the maximum pixel intensity normalized to 100% before applying a colormap.

Acknowledgements

The authors are grateful to Bart Royeaerd and Sven Cederberg for helping with the extensive technical developments needed to perform this work. Support of the operation of the tandem accelerator at Uppsala University by VR-RFI (contract #2019-00191) is gratefully acknowledged. H.J.W. acknowledges support from the Research Council of Norway for the Norwegian Micro and Nano-Fabrication Facility, NorFab (project no. 245963).

Conflict of Interest

The authors declare no conflict of interest.

Data Availability Statement

The data that support the findings of this study are available from the corresponding author upon reasonable request.

Keywords

MeV ion microprobes, particle-induced X-ray emission, Pb–Sn solders, Restriction of Hazardous Substances (RoHS), Sn–Cu solders

Received: June 29, 2022
Revised: November 16, 2022
Published online: January 4, 2023

[1] The Business Research Company, *Electronic Products Market 2021*, **2022**, https://www.thebusinessresearchcompany.com/report/electronic-products-market (accessed: December 2022).
[2] European Parliament and the European Council, Directive 2011/65/EU of the European Parliament and of the Council of 8 June 2011 on the Restriction of the Use of Certain Hazardous Substances in Electrical and Electronic Equipment.
[3] R. Aradhana, S. Mohanty, S. K. Nayak, *Int. J. Adhes. Adhes.* **2020**, *99*, 102596.
[4] L. Li, C. Lizzul, H. Kim, I. Sacolick, J. Morris, *IEEE Trans. Components, Hybrids, Manuf. Technol.* **1993**, *16*, 843.
[5] A. Santamaria, M. E. Muñoz, M. Fernández, M. Landa, *J. Appl. Polym. Sci.* **2013**, *129*, 1643.
[6] W. N. C. Weng, In *Soldering Materials* (Ed.:Eds: A. A. Mohamad), IntechOpen, London, UK **2017**, Ch. 5.
[7] T. Bieler, T. Lee, in *Reference Module In Materials Science And Materials Engineering*, Elsevier, Amsterdam **2017**.
[8] H. R. Kotadia, P. D. Howes, S. H. Mannan, *Microelectron. Reliabil.* **2014**, *54*, 1253.
[9] X. Ma, F. Wang, Y. Qian, F. Yoshida, *Mater. Lett.* **2003**, *57*, 3361.
[10] S. Hayes, N. Chawla, D. Frear, *Microelectron. Reliab.* **2009**, *49*, 269.
[11] J. Ma, G. Chen, X. Li, T. Tanaka, J. Tang, in *7th Int. Conf. on Electronic Packaging Technology*, IEEE, Piscataway, NJ, USA **2006**, pp. 251–261.
[12] H. Moayedi, L. Sun, L. Zhang, *Adv. Mater. Sci. Eng.* **2015**, *2015*, 639028.
[13] Y. Qiao, H. Ma, F. Yu, N. Zhao, *Acta Mater.* **2021**, *217*, 117168.
[14] X. Bi, X. Hu, Q. Li, *Mater. Sci. Eng. A* **2020**, *788*, 139589.
[15] H. Wang, X. Hu, X. Jiang, *Mater. Character.* **2020**, *163*, 110287.
[16] S. Fürtauer, D. Li, D. Cupid, H. Flandorfer, *Intermetallics* **2013**, *34*, 142.
[17] N. Hussein, *Materials Science and Engineering,* International Energy and Environment Foundation, Najaf, Iraq **2017**, p. 146.
[18] S. Chattopadhyay, S. Srikanth, *J. Phase Equilib.* **1994**, *15*, 553.
[19] M. Nastasi, J. Mayer, Y. Wang, in *Ion Beam Analysis: Fundamentals And Applications*, CRC Press, Boca Raton, FL **2015**, pp. 141–170.

[20] M. H. B. Breese, D. N. Jamieson, P. J. King, in *Materiasl Analysis Using A Nuclear Microprobe*, Wiley, New York **1966**.
[21] H. Whitlow, M. Q. Ren, in *Ion Beam Analysis: Fundamentals And Applications*, CRC Press, Boca Raton, FL **2015**, pp. 309–337.
[22] G. Demortier, D. Decroupet, S. Mathot, *Nucl. Instrum. Methods Phys. Res. B: Beam Interact. Mater. Atoms* **1991**, *54*, 346.
[23] A. Soares, P. Valério, R. Silva, L. Alves, M. Araújo, **2010**.
[24] J. Weber, T. Beier, U. Diehl, D. Lambrecht, H. Mommsen, F. Pantenburg, *Nucl. Instrum. Methods Phys. Res. B: Beam Interact. Mater. Atoms* **1990**, *50*, 221.
[25] Q. Lemasson, B. Moignard, C. Pacheco, L. Pichon, M. Filomena Guerra, *Talanta* **2015**, *143*, 279.
[26] Z. Szoboszlai, Z. Kertész, Z. Szikszai, A. Angyal, E. Furu, Z. Török, L. Daróczi, Á. Kiss, *J. Hazard. Mater.* **2012**, *203–204*, 308.
[27] R. Meesat, W. Sudprasert, E. Guibert, L. Wang, T. Chappuis, H. J. Whitlow, *Nucl. Instrum. Methods Phys. Res. B: Beam Interact. Mater. Atoms* **2017**, *404*, 106.
[28] W. Sudprasert, R. Meesat, H. J. Whitlow, H. Udeogu, A. B. De Vera, N. Deoli, *Nucl. Instrum. Methods Phys. Res. B: Beam Interact. Mater. Atoms* **2019**, *450*, 347.
[29] C. Ryan, *Nucl. Instrum. and Meth. B* **2001**, *181*, 170.
[30] C. Ryan, D. Jamieson, C. Churms, J. Pilcher, *Nucl. Instrum. Meth. B* **1995**, *104*, 157.
[31] C. G. Ryan, *Int. J. Imag. Syst. Technol.* **2000**, *11*, 219.
[32] N. Mookam, P. Tunthawiroon, K. Kanlayasiri, *9th Int. Conf. on Mechatronics and Manufacturing (ICMM 2018), volume 361 of IOP Conf. Series: Materials Science and Engineering*. IOP Publishing, Bristol, UK **2018**, p. 012008.
[33] M. N. Croker, R. S. Fidler, R. W. Smith, *Proc. R. Soc. A* **1973**, *335*, 15.
[34] M. Zhao, L. Zhang, Z.-Q. Liu, M.-Y. Xiong, L. Sun, *Sci. Technol. Adv. Mater.* **2019**, *20*, 421.
[35] L. McKeon, *Ph.D. Thesis*, Dublin City University, **2014**.
[36] G. Nagy, H. J. Whitlow, D. Primetzhofer, *Nucl. Instrum. Meth. Phys. Res. B: Beam Interact. Mater. Atoms* **2022**, *533*, 66.
[37] H. J. Whitlow, M. Ren, J. A. van Kan, F. Watt, D. White, *Nucl. Instrum. Meth. Phys. Res. B: Beam Interact. Mater. Atoms* **2007**, *260*, 28.
[38] C. A. Schneider, W. S. Rasband, K. W. Eliceiri, *Nat. Methods* **2012**, *9*, 671.